Full year cycle of desert dust spectral optical thickness and precipitable water vapor over Alexandria, Egypt

I. Sabbah

Department of Physics, Faculty of Science, Alexandria University, Alexandria, Egypt

Charles Ichoku

Science Systems and Applications, Inc., NASA Goddard Space Flight Center, Greenbelt, Maryland

Yoram J. Kaufman and Lorraine Remer

Laboratory for Atmospheres, NASA Goddard Space Flight Center, Greenbelt, Maryland

Abstract. We study the annual cycle of dust loading in Alexandria, Egypt. Observations were performed from December 1997 to November 1998, including during the Kamaseen storms of March 1998. A ground-based, manual Sun photometer was used to measure aerosol optical thickness (τ_a) at four spectral bands in the 340-870 nm wavelength range (namely 340, 440, 675, 870). Total precipitable water vapor (W) was also measured simultaneously, based on the 936 nm channel measurements and extrapolations of the aerosol optical thickness from the neighboring 675 and 870 nm channels. Aerosol optical thickness τ_a at all the four spectral bands were very high (averaging 2.0-4.0) during the Kamaseen storms of late March 1998. Correspondingly, the Ångström wavelength exponent α of the optical thickness fell close to zero during that time, implying a substantial increase in dust. Overall, the monthly mean and median aerosol optical thickness were highest during January-May and lowest in June-October. During the January-May period total precipitable water vapor and Ångström exponent were lower than during the June-October period. There is a high correlation between the Ångström exponent and the optical thickness (r=0.63), with α ranging from 0.0 to 0.5 for $\tau_a > 1.0$, indicating high dust concentration. Trajectory analysis shows that the presence of dust was associated with air masses arriving predominantly from the Sahara or North Africa. No significant correlation was found between the optical thickness and the precipitable water vapor. These basic systematic observations are vital for assessing dust climatology in this important part of the world and also for validating satellite observations and dust transport models.

1. Introduction

Routine daily observations of the ambient aerosol (e.g., desert dust) in the vertical column taken from the ground and from satellites are required to obtain a regional and global aerosol budget [*Flowers et al.*, 1969; *Kaufman and Fraser*, 1983]. This information can then be used to evaluate models of dust transport and radiative forcing of climate [*Tegen et al.*, 1996], and of the climatic response to the presence of dust [*Alpert et al.*, 1998]. Ground-based measurements can establish the climatology of the aerosol properties [*WMO*, 1983; *Shettle*, 1984; *d'Almeida et al.*, 1991] and can be

used to validate and extend the application of satellite data [*Tanré et al.*, 1988; *Tanré and Legrand*, 1991]. Studies on dust distribution in the Sahel in relation to vegetation remote sensing were conducted by *Holben et al.* [1991]. Long-range dust transport can affect atmospheric composition, clouds, surface vegetation, and intake of minerals into the oceans [*Prospero*, 1981; *Levin et al.*, 1996; *Dentener et al.*, 1996]. Alexandria, Egypt, is on the transport pathway of the Saharan dust to the eastern Mediterranean and Europe. The climatology of the dust events in Alexandria is important to understand the impact of dust on the climate in this region. Here, using systematic measurements of dust and water vapor in one location in Alexandria, we establish a 1 year climatology of the dust spectral optical thickness and its relationship to the presence of water vapor in the atmosphere.

2. Study Site (Alexandria, Egypt)

Alexandria (longitude = 30.1° East, latitude = 31.3° North), the site of the experiment reported in this paper, is located on the southeastern coast of the Mediterranean Sea. It is the second largest city in Egypt, holds more than one third of the Egyptian national industries, is a very important historical city, and is considered as the principal seaside summer resort on the Mediterranean [Frihy et al., 1996]. It is therefore a very important location to study the climatic influences of dust and global change dynamics.

Alexandria lies at the junction of several climate systems, including the Mediterranean and the Saharan systems. It potentially can be impacted not only by those systems and their combined effect but also by long-range transport of materials from distant sources. As a result, it is characterized by a complex synoptic meteorology, which changes with time of year [Moulin et al., 1998].

3. Methodology

3.1. Measurements and Calibration

Portable Sun photometers (Microtops II, manufactured by Solar Light Company, Philadelphia, Pennsylvania) are being used in various parts of the world to measure the aerosol optical thickness (AOT or τ_a) at 340, 440, 675, and 870 nm, and total precipitable water vapor (W) using the 936 nm channel. In this experiment, measurements were conducted in Alexandria, Egypt, during the period from December 1997 to November 1998. These were done on days that were as cloud free as possible to avoid the contamination of the measurements by cloud. To ensure the stability of the instrument and the measuring conditions, the measurements were taken in sets of 3 or more in quick succession. One or several such sets of measurements were obtained per day.

The Microtops II Sun photometer used for this work was calibrated against a reference Sun photometer before, during, and close to the end of the measurement period. The reference instrument is the master automatic tracking Sun photometer/sky radiometer measuring instrument (CIMEL Electronique 318A) located at the National Aeronautics and Space Administration (NASA) Goddard Space Flight Center (GSFC), Greenbelt, Maryland. This reference instrument, which is part of the global Aerosol Robotic Network (AERONET) [Holben et al., 1998], is itself regularly calibrated using Langley plots at the pristine mountain top of the National Oceanic and Atmospheric Administration (NOAA) Observatory at Mauna Loa, Hawaii. Approximately every 15 min, the reference Sun photometer routinely makes direct Sun measurements at 340, 380, 440, 500, 670, 870, 936, and 1020 nm wavelengths, from which it derives aerosol optical thickness τ_a. These were used to calibrate the corresponding Microtops II aerosol

channels. Furthermore, the CIMEL 936 nm channel was used to derive the total precipitable water vapor amount, which was also used in turn to calibrate the Microtops II water vapor measurements. The calibration measurements were carried out on days that were completely cloud free (at least as far as the eye can see), with the Sun high in the sky, and with low and stable aerosol concentration. These measures were taken to ensure contamination-free conditions. On any given calibration day, measurements were made with the Microtops instrument simultaneously with the reference instrument during at least 1 hour, to allow for sufficient redundancy for accuracy verification.

The calibration of each of the aerosol channels (340, 440, 675, 870 nm) of the Microtops is based on the Beer-Lambert-Bouguer law:

$$V_\lambda = V_{0\lambda} D^{-2} \exp(-\tau_\lambda M), \qquad (1)$$

where for each channel (wavelength) V_λ is signal measured by the instrument at wavelength λ, $V_{0\lambda}$ is extraterrestrial signal, D is the Earth-Sun distance in astronomical units at the time of observation, τ_λ is total optical thickness ($\tau_\lambda = \tau_{a\lambda} + \tau_{R\lambda} + \tau_{O_3\lambda}$), $\tau_{a\lambda}$ is aerosol optical thickness, $\tau_{R\lambda}$ is Rayleigh (air) optical thickness, $\tau_{O_3\lambda}$ is ozone optical thickness, and M is the optical air mass. For the 936 nm (water vapor) channel, in addition to the contribution of aerosol and molecular scattering to the optical thickness, there is a nonlinear contribution from water vapor. Thus the equation becomes [Reagan et al., 1995]

$$V_w = V_{0w} D^{-2} \exp[-\tau_w M - k(WM)^b], \qquad (2)$$

where V_w, V_{0w}, D, τ_w, and M remain as defined in equation (1), except that subscript w (instead of λ) is used to designate the wavelength for the 936 nm channel because of the significant water vapor influence on this channel. W is vertical water vapor column thickness, and k and b are instrument constants numerically derived for the 936 nm filter. The Rayleigh and ozone optical thicknesses $\tau_{R\lambda}$ and $\tau_{O_3\lambda}$ are obtained from atmospheric models:

$$\tau_{R\lambda} = R_4 \exp(-h/29.3/273), \qquad (3)$$

$$\tau_{O_3\lambda} = \text{Ozabs} * \text{DOBS}/1000, \qquad (4)$$

where

$$R_4 = 28773.6(R_2 * (2 + R_2) * \lambda^{-2})^2, \qquad (5)$$

$$R_2 = 10^{-8} \left(8342.13 + \frac{2406030}{(130 - \lambda^{-2})} + \frac{15997}{(38.9 - \lambda^{-2})} \right), \qquad (6)$$

h is altitude of the place of observation in meters, and λ is wavelength in microns. (For further information on

Table 1. Microtops II Sun Photometer Calibration Coefficients (V_0) at Different Wavelengths

DATE	$V_0(340)$	$V_0(440)$	$V_0(675)$	$V_0(870)$	$V_0(936)$
MANUF.	3155.81	1199.91	1160.96	832.14	1802.63
06 October 1997	3363.85	1181.87	1172.01	834.56	2556.55
22 May 1998	3224.35	1153.99	1144.74	815.77	1918.80
16 March 1999	3306.91	1106.17	1065.71	806.27	1922.30
30 March 1999	3286.78	1109.30	1063.76	804.07	1810.92
31 March 1999	3282.74	1112.90	1063.78	805 48	1812.34

From the manufacturer (MANUF) and from calibrations conducted on the indicated dates against the Cimel Sun photometer (of the AERONET network) located at NASA GSFC.

$\tau_{R\lambda}$ computation, see for example, Edlén [1966], Teillet [1990], and Bodaine et al. [1999]). Ozabs is ozone absorption cross section, extracted from a look-up table based on wavelength [e.g., Molina and Molina, 1986, Vigroux, 1953]; and DOBS is Ozone amount in Dobson units, extracted from a look-up table based on latitude and date of observation [e.g., London et al., 1976]. $V_{0\lambda}$ differs for each instrument and changes slowly with time. We find the actual values of $V_{0\lambda}$ by substituting τ_a derived from the reference Sun photometer into equation (1) or (2) for the corresponding channel of the Microtops.

Table 1 shows a list of the original $V_{0\lambda}$ values as given by the manufacturer of the Microtops Sun photometer, and those determined from all the calibrations performed for the instrument used in this experiment. Each of the $V_{0\lambda}$ values is the mean of several values determined on a given calibration day. The uncertainty in $V_{0\lambda}$ is estimated by its coefficient of variation (CV), which is standard deviation/mean. CV indicates the combined uncertainty of the atmosphere, instrument, and the repeatability of the calibration procedure. The CV values (in percent) corresponding to the $V_{0\lambda}$ in Table 1 are shown in Table 2. Based on these results, it can be inferred that the calibrations of the visible/near-infrared (NIR) channels (440, 675, and 870 nm) are at least twice more reliable than those of either the ultraviolet (340 nm) or the water vapor absorption (936 nm) channel. A similar pattern of relationship between channels was also observed by Holben et al. [1998].

3.2. Data Adjustment

To ensure good quality control, prior to adjustment, the Alexandria measurements were subjected to filtering to remove bad data. This is because although all effort was made to take the measurements during apparent cloud free conditions, nevertheless since they were obtained manually, it was still possible for bad measurements to occur, perhaps because of poorly visible clouds or inaccurate pointing of the instrument optical train to the Sun. To avoid such contamination, advantage was taken of the sets of measurements in triplets (or more), which are at most a couple of minutes apart, to perform the filtering. The criterion used was that if successive τ_a values changed by more than 100% per minute in any wavelength, the entire line of data where the large difference occurred is eliminated. The filtering was followed by the actual data adjustment using the instrument calibration coefficients

For a given Microtops Sun photometer the calibration parameters $V_{0\lambda}$ obtained from two consecutive calibrations, are used to adjust all data measured in the intervening period. First, sets of $V_{0\lambda}$ from successive calibrations are linearly interpolated with time to compute calibrated sets of $V_{0\lambda}$ for all the intervening date/time of regular observations. Then, the interpolated set of $V_{0\lambda}$ for each time of observation is substituted in equation (1) or (2), to compute, for each wavelength, the adjusted τ_λ from which the adjusted $\tau_{a\lambda}$ is derived $(\tau_{a\lambda} = \tau_\lambda - \tau_{R\lambda} - \tau_{O_3\lambda})$. Adjustment for $\tau_{a\lambda}$ at 340,

Table 2. Percent Coefficient of Variation (Standard Deviation/Mean) of the Calibration Coefficients (V_0) for the Different Wavelengths and Calibration Dates

DATE	$CV_{(340)}$	$CV_{(440)}$	$CV_{(675)}$	$CV_{(870)}$	$CV_{(936)}$
06 October 1997	1.84	0.79	0.56	0.36	1.23
22 May 1998	0.99	0.47	0.49	0.56	0.78
16 March 1999	0.28	0.31	0.23	0.36	0.45
30 March 1999	0.70	0.30	0.28	0.26	1.77
31 March 1999	0.76	0.14	0.25	0.08	0.29

contribution to the optical thickness at 936 nm, τ_{aw}, is determined by extrapolation from the $\tau_{a\lambda}$ values at 675 and 870 nm as follows:

$$\tau_{aw} = \tau_{a870} * \exp[\alpha_{870/675} * \ln(936/870)], \qquad (7)$$

where

$$\alpha_{870/675} = \frac{\ln(\tau_{a870}/\tau_{a675})}{\ln(870/675)}. \qquad (8)$$

Here $\alpha_{870/675}$ is the Ångström exponent derived using only the 870 and 675 nm channels. It should be mentioned that the extrapolation method used here is an improvement over the internal determination of τ_{aw} by the Microtops II Sun photometer (which is done simply by multiplying τ_{a870} by 0.91, based on the presumption that corresponding values of AOT at 870 nm and at 936 nm wavelengths are always related by this constant ratio). Once τ_{aw} is extrapolated, the adjusted value of W is derived by combining equations (1) and (2) and substituting the adjusted τ_{a870} and τ_{aw} as well as the other required parameters.

4. Results

4.1. Analysis of AOT and W Data

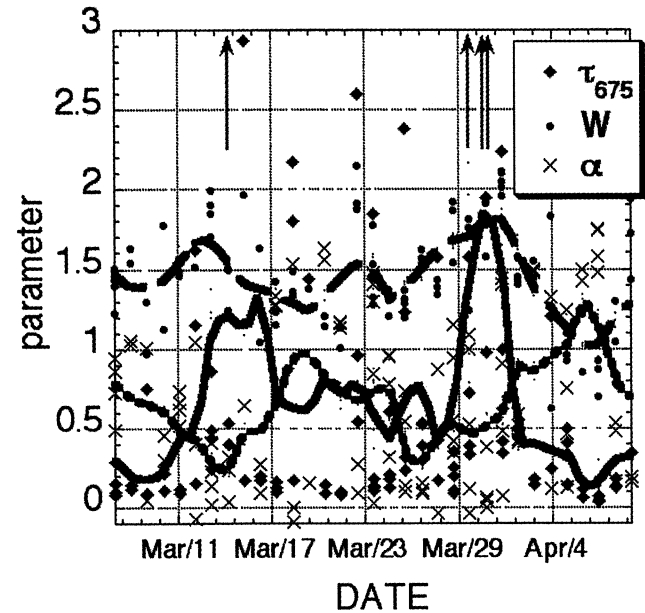As a result of the calibration, the absolute accuracy of the measurements in this work is expected to be ±0.02

Plate 1. Time series of the aerosol optical thicknesses (AOT). (top) Monthly averages of the AOT at 675 nm, bars; the Ångström exponent, red line; and the water vapor, blue line. The AOT median, green line; and the 90% and 10% percentiles are also plotted. December through May 1998 experienced lower precipitable water vapor, lower Ångström exponent, and higher aerosol concentration than the rest of the year, indicating the presence of dry, dusty air (note that the averages for May could have been biased, because they were based on very small samples, as revealed by the data gap in the bottom panel). Bottom panel shows the hourly averages of AOT at 675 nm, Ångström exponent, and total precipitable water vapor.

440, 675, and 870 nm wavelengths is straightforward using equation (1). For $\tau_{a\lambda}$ at 936 nm (τ_{aw}) and for the column water vapor (W), the adjustment cannot be done directly using equation (2), because one is needed to compute the other. A different procedure is used to adjust them. First, the adjusted value of the aerosol

Plate 2. Time series of AOT at 675 nm (τ_{a675}), the total precipitable water vapor W, and the Ångström exponent α during the Kamaseen storms of March 1998. The individual measurements are shown (dots) as well as the five point running averages (lines). The arrows indicate values of the optical thickness larger than 3.0. Note the inverse dependence of the aerosol optical thickness and the Ångström exponent, indicating that the elevated aerosol concentrations are caused by dust.
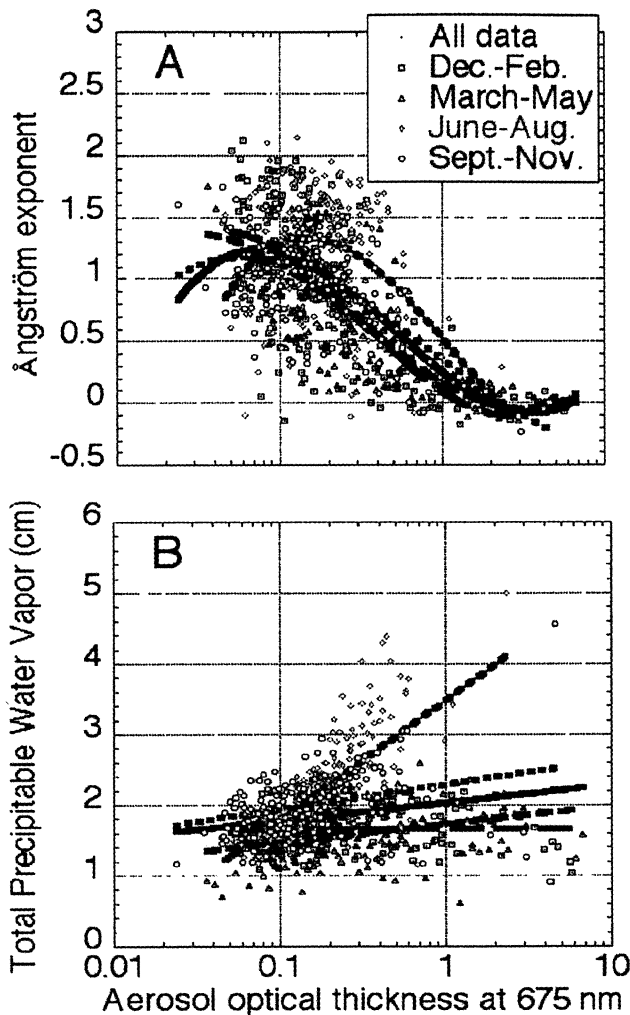
Plate 3. Scatterplots of the Ångstrom (wavelength) exponent of the aerosol optical thickness (top) and the total precipitable water vapor (bottom) as a function of AOT at 675 nm. The plots are given for four seasons: December-February (blue), March-May (green), June-August (orange), and September-November (red). Black lines represent all the data. In all the seasons, elevated values of the optical thickness correspond to lower (in magnitude) values of the Ångström exponent, thereby indicating the presence of dust.

for the optical thickness at 440-870 nm and ±0.2 cm for W, with a precision 4 times better than the corresponding measured values. The error at 340 nm is expected to be 0.03. To simplify the data analysis, hourly averaging was performed, such that measurements taken during each hourly period were averaged to create one data point. Plate 1 presents the time series of the aerosol optical thickness, the precipitable water vapor, and the Ångström exponent. The Ångström exponent is defined as

$$\alpha_{870/440} = -\frac{\ln(\tau_{a870}/\tau_{a440})}{\ln(870/440)}. \tag{9}$$

The data show that December 1997 through May 1998 experienced lower precipitable water vapor, lower Ångström exponent, and higher aerosol concentration than the rest of the year, indicating the presence of dry, dusty air. Strong dust episodes, indicated by high values of the 90 percentile of the optical thickness in Plate 1, occurred in March and May. Note, however, that because of the data gap that occurred in May (as can be very easily perceived in the bottom panel), the averages for that month may not be representative, since they were computed from very small samples covering only the beginning of the month. The bottom panel of Plate 1 shows time series of the individual hourly measurements. The dust episodes are indicated by the spikes in the optical thickness curve. The main dust storms occurred in March, and the corresponding data segment is replotted as a function of time in Plate 2. Note the inverse dependence of the aerosol optical thickness and the Ångström exponent, indicating that elevated aerosol concentrations are caused by dust. Four measurements in that period of time showed aerosol optical thickness larger than 3.0.

Scatterplots of the Ångström wavelength exponent (α) of the optical thickness and precipitable water vapor (W), as a function of the aerosol optical thickness at 675 nm, are shown in Plate 3. The period of the measurements is divided into four seasons: December-
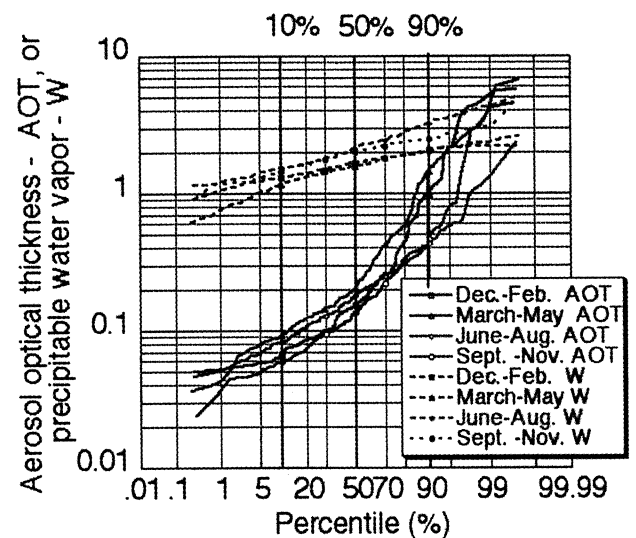

Plate 4. Cumulative distributions of the spectral optical thickness (AOT) at 675 nm and the total precipitable water vapor for the four seasons. Note that half of the measurements correspond to AOT of less than 0.2 for all the seasons. The difference in dust loading between these four periods is represented by the strong increase in the AOT for cumulative distribution of 90% in December-May. Whereas 10% of the cases for December-May have AOT ≥ 1, the highest 10% of the cases for June-August correspond to only AOT > 0.4. The water vapor distributions in the four seasons are similar to one another.

February, March-May, June-August, and September-November. The curve fitting for the top panel is based on a third-degree polynomial with $\ln(\tau_{a675})$ as the independent variable, while the lines in the bottom panel were fitted by linear regression. All the seasons show a very similar dependence of $\alpha_{870/440}$ on AOT with a nonlinear correlation of between 0.4 and 0.7. The Ångström exponent $\alpha_{870/440}$ varies from 1 to 2 for small AOT, typical of urban (including local) air pollution aerosol, as observed in other urban areas [Kaufman and Fraser, 1983], whereas the values are around zero for heavy dust (large AOT). The bottom panel of Plate 3 shows no clear relationship between the total precipitable water vapor and the AOT except for the period of June-August, for which there is a marked positive linear correlation. This is suggestive of hygroscopicity greater than that of dust Since that period also showed extremely few cases of high τ_a values, the aerosol occurring during that season is characteristic not of dust but of anthropogenic aerosol (air pollution), such as has been observed in the eastern coast of the United States [Hegg et al., 1997].

Even though Alexandria is on the fringes of the Sahara desert, the cumulative distribution of the AOT (Plate 4) shows that half of the measurements corre-spond to clean conditions, with optical thickness smaller than 0.2 at 675 nm. In December-May the highest 10% of the dusty conditions correspond to $\tau_a > 1.0$, while in June-November the highest 10% correspond only to $\tau_a > 0.4$. These situations will be explained by the air-mass transport scenarios from back-trajectory analysis discussed below.

4.2. Analysis of Air-Mass Back Trajectories

To explain the trends shown by the AOT and W data, an analysis of the air-mass flow patterns in the area was conducted. This involved the analysis of the 5 day air-mass back trajectories generated from the meteorological data provided by the National Centers for Environmental Prediction (NCEP). Since it would be difficult to conduct such a complex and daily variable analysis for the entire year of the experiment, certain days spread over the different seasons of the year were selected for study. The selection was made in a semi-random manner; and effort was made to select days representative of the four periods of the year identified above (Plate 3), loaded with different levels of AOT and W. Table 3 shows the selected dates, with some τ_{a675} and corresponding $\alpha_{870/440}$ as well as W measurements. For each of the selected days, individual mea-

Table 3. Characterization of Aerosol Types and Analysis of NCEP 5 Day Back Trajectories Over Alexandria, Egypt, for Selected Dates

Date	Time(UT)	τ_{a675}	$\alpha_{870/440}$	W	AerosolType	Below 1 km	1 to 5 km	Above 5 km
16 December 1997	11:52:28	0.11	0.44	1.76	mixed	WE	WE	WE
01 January 1998	09:02:16	0.96	-0.02	1.74	dust	WE	NA	S
05 January 1998	09:16:57	0.10	1.59	1.81	pollution	WE	WE	WE
28 January 1998	10:20:27	4.03	0.08	0.98	dust	S	NA	NA
23 February 1998	12:20:40	0.06	1.82	1.60	clean	O	WE	WE
15 March 1998	08:01:27	0.55	0.23	1.51	dust	NA	S	S
15 March 1998	10:14:15	6.06	0.03	1 30	dust	NA	S	S
31 March 1998	11:41:00	6.76	0.00	1.70	dust	NA	NA	NA
07 April 1998	10:13:34	0.04	1 76	0.92	clean	O	O	O
28 April 1998	08:40:18	2.69	0.14	1.87	dust	WE	WE	NA
28 April 1998	11:05:36	0.23	1.45	1.72	pollution	WE	WE	NA
09 May 1998	11:51:16	1.45	0.01	2.34	dust	WE	S	S
20 June 1998	10:01:31	0.07	0.26	1.18	mixed	WE	WE	WE
09 August 1998	08:46:42	0.46	1.55	4.03	pollution	EE	ME	ME
21 August 1998	07:28:37	0.07	1.70	1.57	pollution	EE	WE	WE
13 September 1998	06:43:12	0.36	1.34	2.51	pollution	EE	WE	WE
17 September 1998	09:49:58	0.05	0.79	1.96	clean	WE	WE	WE
16 October 1998	09:36:12	0.07	0.81	1.94	mixed	WE	WE	NA
22 October 1998	08:33:36	2.97	-0.12	1.58	dust	EE	S	S
25 October 1998	08:52:05	0.84	0.08	2 23	dust	WE	S	S
03 November 1998	10:53:58	0.08	1.02	2.06	pollution	WE	WE	WE
22 November 1998	07:38:36	0.98	0.15	1.81	dust	O	O	S
24 November 1998	09:32:54	0.03	0.42	1.15	clean	NA	S	WE
09 December 1998	07:09:05	0.55	0.07	2 01	dust	WE	S	S

In column 6 the aerosol is categorized into "clean" for $\tau_{a675} \leq 0.06$, while for $\tau_{a675} > 0.06$, it is "dust" when $\alpha_{870/440} < 0.25$, "pollution" when $\alpha_{870/440} > 1.0$, and "mixed" otherwise. The acronyms in columns 7 to 9 represent the directions of approach of the trajectories at three altitude ranges: west Europe (WE), east Europe (EE), Middle East (ME), Sahara (S), northwest Africa (NA), and stagnant or no wind (O). The data in rows 6, 9, 16, and 18 correspond to the dates of the back trajectory and TOMS AI shown in Plates 5 and 6, respectively.

surements, rather than the daily averages, are shown. This is because although for most days the measurements did not vary significantly throughout the day, for certain days however, such as 15 March 1998, there was a very large difference between the measurements obtained at about 0800 UT and those measured just a couple of hours later. A similar difference was observed also on 28 April 1998. Therefore, showing only daily averages would have obscured such interesting diurnal variabilities.

An attempt was made to characterize the aerosol types on the basis of the values of the optical thickness τ_{a675} and the Angstrom exponent $\alpha_{870/440}$. Cases with $\tau_{a675} \leq 0.06$ were classified as "clean" conditions. For those with $\tau_{a675} > 0.06$, further classification was based on the values of Ångström exponent, being categorized as "dust" for $\alpha_{870/440} < 0.25$, "pollution" for $\alpha_{870/440} > 1.0$, and "mixed" otherwise (see Table 3).

Back trajectories were generated from the NCEP system using the NASA Goddard Space Flight Center (GSFC) isentropic trajectory model [Schoeberl et al., 1993; Pickering et al., 1996], which is based on the use of potential temperatures. For each of the selected dates, the back-trajectories were generated at different potential temperature levels, which may be grouped into three altitude ranges, namely, below 1 km, 1-5 km, and above 5 km. The trajectory arrival times were set at 1200 UT. These trajectories were examined and classified according to their directions of approach to Alexandria (see Table 3). Six categories were identified, namely, western Europe (WE), eastern Europe (EE), Middle East (ME), the Sahara (S), northwest Africa (NA), and stagnant air or no wind (O). In spite of the nearness of Alexandria to the Sahara, air masses seldom came directly from the Sahara, and even the few trajectories coming from that direction often occurred at high altitudes. On most of the days studied, the back trajectories show that the air masses ending in Alexandria, especially at the lower levels of the atmosphere, came from western or central Europe. This pattern of air-mass transport has been found to be predominant in this region from previous studies [La Fontaine et al., 1990; Moulin et al., 1998].

In all of the dust cases, the air came from the Sahara or North Africa at least in one of the identified layers. The pollution aerosol came always with at least one of the layers from Europe and was, on the average, associated with 30% higher precipitable water vapor. This is an excellent correspondence. However, it should be mentioned that on 15 March and 28 April 1998, the two τ_{a675} observations at different times of the day differed by a very large margin. This large diurnal variability could have led one to think that the high AOT values that occurred on such days may have been caused by local dust events, or even that they may be faulty values. Although these are quite possible, trajectory analysis helps to visualize the probable scenario under such situations. Plate 5 shows a sample back-trajectory for

each of the four aerosol conditions identified above: (a) "dust" on 15 March, (b) "clean" on 07 April, (c) "pollution" on 13 September, and (d) "mixed" on 16 October. The rows representing these dates are shown in Table 3. Focusing on the event of 15 March (Plate 5a), it is clear that there was a massive dust transport from the Sahara, which reached Alexandria probably in the late morning of that day.

In regard to the precipitable water vapor W levels, since the air masses come most frequently from Europe, they invariably pass over the Mediterranean before reaching Alexandria. This explains why most of the selected days and indeed the entire observations showed substantial water vapor levels.

4.3. Comparison With TOMS Satellite Aerosol Index (AI) Images

One of the most useful applications of the type of ground measurements discussed in this paper is in the validation of satellite retrievals, which themselves offer a spatial view of the phenomenon being measured. The Total Ozone Mapping Spectrometer (TOMS), launched on 2 July 1996, aboard the Earth Probe spacecraft, routinely retrieves a quantity referred to as the aerosol index (AI). This is a measure of the wavelength-dependent change of Raleigh-scattered radiance resulting from the competing effects of scattering and absorption relative to a pure Raleigh atmosphere (for further details, see Herman et al. [1997], Hsu et al. [1999], and Chiapello et al. [2000]). It is pertinent to mention that AI is defined such that positive values generally correspond to ultraviolet (UV) absorbing aerosols, while negative values correspond to nonabsorbing aerosols [Chiapello et al., 2000]. Since the AI is a somewhat different quantity than the AOT, their actual values cannot be compared directly, but their temporal and spatial variability can be compared

Plate 6 shows color-coded images of TOMS AI parameters for the same dates as the back trajectories presented above (Plate 5). The image representing 15 March 1998 shows that there was a dust storm just entering Alexandria from the Sahara on that day. This situation was indicated by the corresponding back trajectory above (Plate 5a). The images for the other 3 days (Plate 6) do not show any indications of absorbing aerosols over Alexandria. To try to understand the dynamics of the evolution of the dust storm that swept over Alexandria on 15 March 1998, a 4 day sequence of the AI images around this date is shown in Plate 7. It is seen that the storm, which affected Alexandria on 15 March, was centered above the Sahara on 13 March, close to the Mediterranean coast of Libya on 14 March, passed over Alexandria on 15 March, and proceeded on its way to the eastern Mediterranean region on 16 March 1998. This is an excellent illustration of the potential for validation of satellite data with the type of measurements reported in this paper. AOT and water vapor data measured with Microtops II Sun

NCEP Back-trajectories
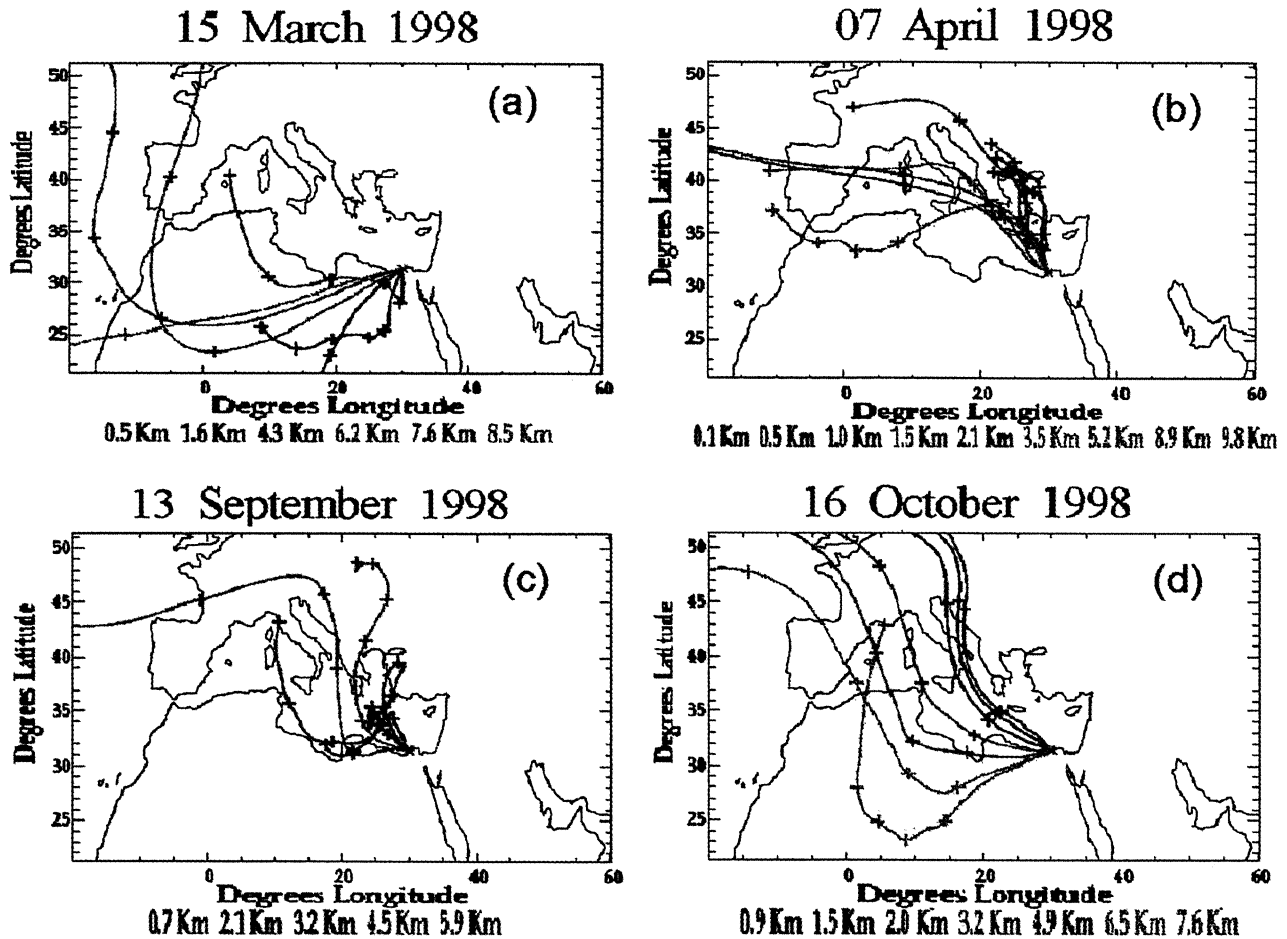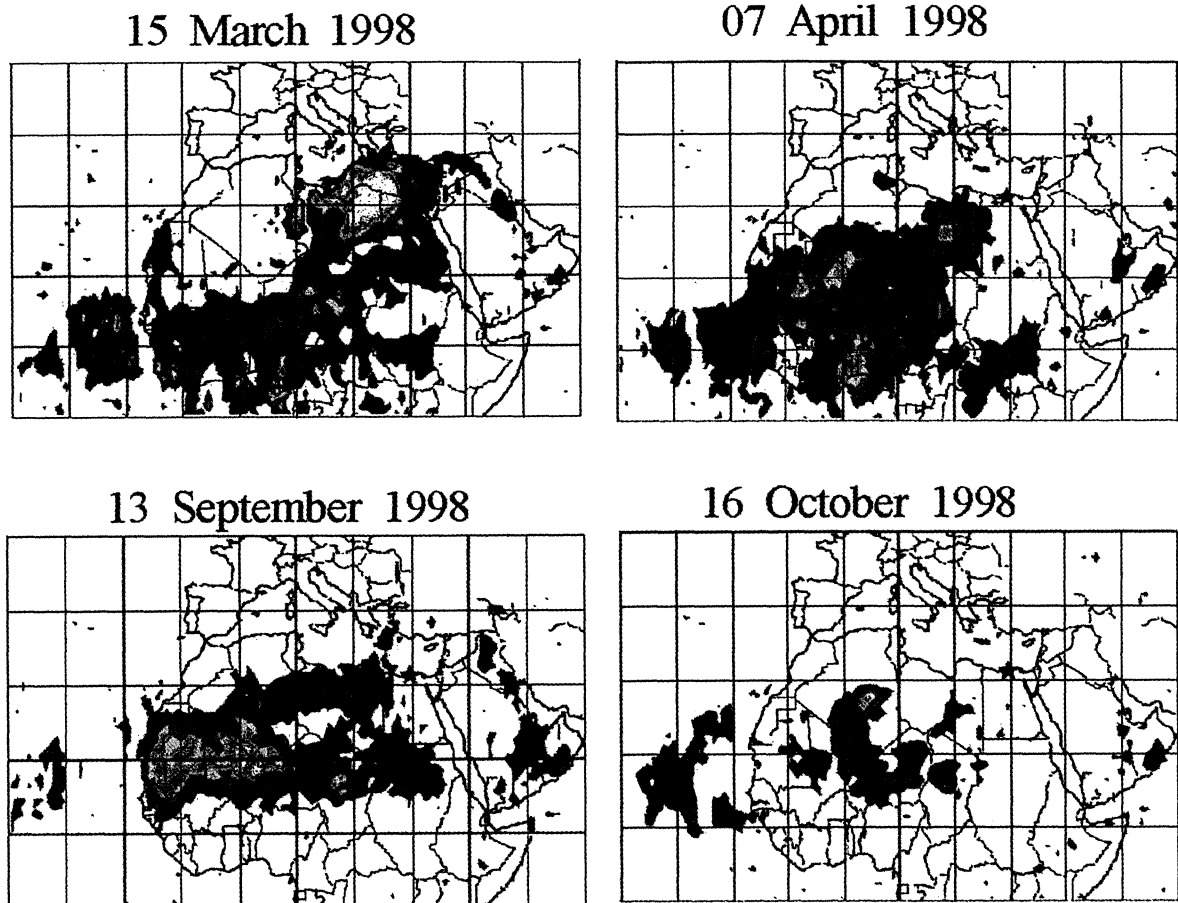
(Crosses mark 24 hour intervals)

15 March 1998

(a)

0.5 Km 1.6 Km 4.3 Km 6.2 Km 7.6 Km 8.5 Km

07 April 1998

(b)

0.1 Km 0.5 Km 1.0 Km 1.5 Km 2.1 Km 3.5 Km 5.2 Km 8.9 Km 9.8 Km

13 September 1998

(c)

0.7 Km 2.1 Km 3.2 Km 4.5 Km 5.9 Km

16 October 1998

(d)

0.9 Km 1.5 Km 2.0 Km 3.2 Km 4.9 Km 6.5 Km 7.6 Km

Plate 5. Sample 5 day back trajectories illustrating typical air-mass flow configurations giving rise to different aerosol situations in Alexandria, Egypt, as identified in this paper: (a) "dust" on 15 March 1998, (b) "clean" on 07 April 1998, (c) "pollution" on 13 September 1998, and (d) "mixed" on 16 October 1998.

Earth Probe TOMS Absorbing Aerosol Index

15 March 1998

07 April 1998

13 September 1998

16 October 1998

★ Position of Alexandria

1.0	1.4	1.8	2.2	2.6	3.0	3.4>

Aerosol Index

Plate 6. Earth Probe TOMS absorbing aerosol index (AI) images corresponding to the dates of the back trajectories shown in Plate 5.
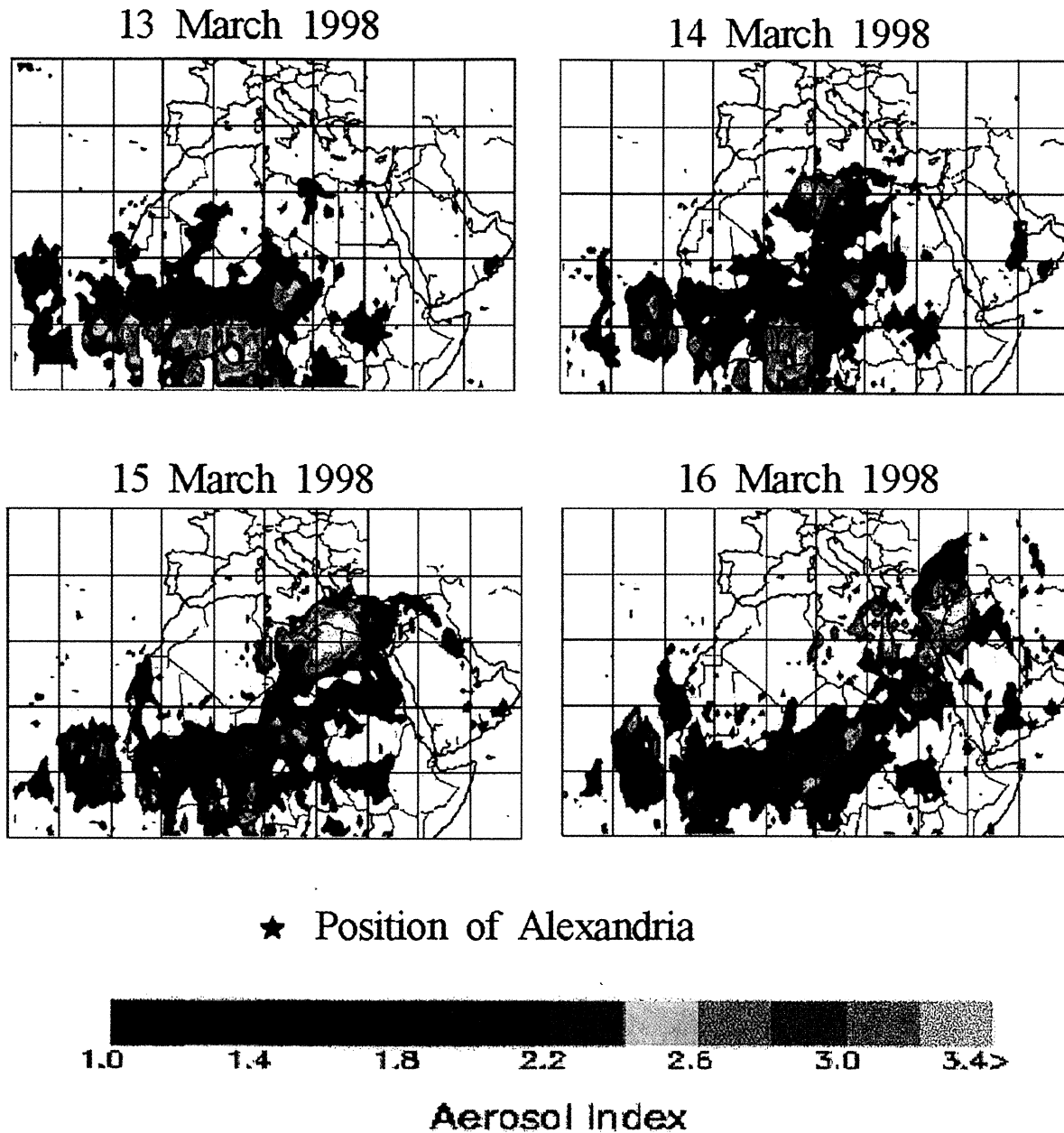
Earth Probe TOMS Absorbing Aerosol Index

13 March 1998

14 March 1998

15 March 1998

16 March 1998

★ Position of Alexandria

Aerosol Index

1.0   1.4   1.8   2.2   2.6   3.0   3.4>

Plate 7. Sequence of Earth Probe TOMS absorbing aerosol index (AI) images for 4 consecutive days around 15 March 1998, showing the displacement of the dust storm that swept through Alexandria, Egypt, on that day.

photometers are currently being used to validate AOT and water vapor retrievals from the new Moderate-resolution Imaging Spectroradiometer (MODIS) instrument (aboard the Terra spacecraft) not only for Alexandria, Egypt, but also for many other parts of the world. The result of those efforts will be published in future papers.

5. Conclusions

We have measured 750 hourly sequences of the spectral optical thickness of aerosols in Alexandria, Egypt, simultaneously with measurements of the total precipitable water vapor, using passive remote sensing in five spectral bands lying in the 340-936 nm wavelength range. Almost a full annual cycle (December 1997 to November 1998) of data has been reported. The observation period includes the 1998 Kamaseen storm season. The main results obtained from this study are as follows. (1) The Ångström wavelength exponent α was in the range of 1 to 2 during periods with low optical thickness but was around zero during the Kamaseen storms characterized by heavy dust with optical thickness above 1.0. This latter situation corresponds to cases when the air-mass trajectories came mainly from the Sahara or from North Africa. (2) The climatology of the aerosol optical thickness indicates that half of the measurements gave aerosol optical thickness values of $\tau_a < 0.2$. The highest 10% of the optical thickness values at 675 nm wavelength are $\tau_a \geq 1$ during the period December to May, but barely above 0.4 during the rest of the year.

References

Alpert, P., Y. J. Kaufman, Y. Shay-El, D. Tanre, A. da Silva, S. Schubert, and Y. H. Joseph, Quantification of dust-forced heating of the lower troposphere, *Nature, 395*, 367–370, 1998.

Bodhaine, B. A., N. B. Wood, E. G. Dutton, and J. R. Slusser, On Rayleigh optical depth calculations, *J. Atmos. Oceanic Technol., 16*, 1854–1861, 1999.

Chiapello, I., P. Goloub, D. Tanre, A. Marchand, J. Herman, and O. Torres, Aerosol detection by TOMS and POLDER over oceanic regions, *J. Geophys. Res., 105*, 7133–7142, 2000.

d'Almeida, G. A., P. Koepke, and E. P. Shettle, *Atmospheric Aerosols, Global Climatology and Radiative Characteristics*, A. Deepak, Hampton, Va., 1991.

Dentener, F J., G. R. Carmichael, Y. Zhang, J. Lelieveld and P. J. Crutzen, Role of mineral aerosol as a reactive surface in the global troposphere, *J. Geophys. Res., 101*, 22,869–22,889, 1996.

Edlen, B., The refractive index of air, *Metrologia, 2*, 71–80, 1966.

Flowers, E. C., R. A. McCormick, and K. R. Kurfis, Atmospheric turbidity over the United States, 1961–1966, *J. Appl. Meteorol., 8*, 955–962, 1969.

Frihy, O. E., K. M. Dewidar, and M. M. El-Raey, Evaluation of coastal problems at Alexandria, Egypt, *Ocean Coastal Manage., 30*, 281–295, 1996.

Hegg, D. A., J. Livingston, P. V. Hobbs, T. Novakov, and P. Russell, Chemical apportionment of aerosol column optical depth off the mid-Atlantic coast of the United States, *J. Geophys. Res., 102*, 25,293–25,303, 1997.

Herman, J R., P. K. Barthia, O. Torres, C. Hsu, C. Seftor, and E Celarier, Global distribution of UV absorbing aerosol from Nimbus 7/TOMS data, *J. Geophys. Res., 102*, 16,911–16,922, 1997.

Holben, B. N., T. F. Eck, and R. S. Fraser, Temporal and spatial variability of aerosol optical depth in the Sahel region in relation to vegetation remote sensing, *Int. J. Remote Sens., 12*, 1147–1163, 1991.

Holben, B. N., et al., AERONET – A Federated Instrument Network and Data Archive for Aerosol Characterization, *Remote Sens. Environ., 66*, 1–16, 1998.

Hsu, C., J. R. Herman, O. Torres, B. N. Holben, D. Tanre, T F. Eck, A Smirnov, B. Chatenet, and F. Lavenu, Comparisons of the TOMS aerosol index with Sun photometer aerosol optical thickness: Results and applications, *J. Geophys. Res., 104*, 6269–6279, 1999.

Kaufman, Y. J. and R. S. Fraser, Light extinction by aerosol during summer air pollution, *J. Appl. Meteorol., 22*, 1694–1706, 1983.

La Fontaine, C. V., R. A. Bryson, and W. M. Wendland, Airstream regions of North Africa and the Mediterranean, *J. Clim., 3*, 366–372, 1990.

Levin, Z , E Ganor and V. Gladstein, The effect of desert particles coated with sulfate on rain formation in the eastern Mediterranean, *J. Appl. Meteorol., 35*, 1511–1523, 1996

London, J., R. D Bojkov, S Oltmans, and J. I. Kelley, Atlas of the Global Distribution of Total Ozone July 1957 – June 1967, *NCAR Tech. Note 133+STR*, 276 pp., Nat. Cent. for Atmos. Res., Boulder, Co., 1976.

Molina, L. T., and M. J Molina, Absolute absorption cross sections of ozone in the 185– to 350–nm wavelength range, *J. Geophys. Res., 91*, 14,501–14,508, 1986.

Moulin, C , et al., Satellite climatology of African dust transport in the Mediterranean atmosphere, *J. Geophys. Res., 103*, 13,137–13,144, 1998.

Pickering, K. E., A. M. Thompson, D. P. McNamara, M. R. Schoeberl, H. E. Fuelberg, R. O. Loring, M. V. Watson, K. Fakhruzzaman, and A. S. Bachmeier, TRACE–A trajectory intercomparison, 1, Effects of different input analyses, *J. Geophys. Res., 101*, 23,909–23,925, 1996.

Prospero, J. M., Eolian transport to the world ocean, in *The Sea, vol VII, The Oceanic Lithosphere*, edited by C. Emiliani, pp. 801–874, John Wiley, New York, 1981.

Reagan, J., K. Thome, B. Herman, R. Stone, J. Deluisi, and J. Snider, A comparison of columnar water-vapor retrievals obtained with near-IR solar radiometer and microwave radiometer measurements, *J. Appl. Meteorol., 34*, 1384–1391, 1995.

Schoeberl, M. R., S. D. Doiron, L. R. Lait, P. A. Newman, and A. J. Krueger, A simulation of the Cerro Hudson SO_2 cloud, *J. Geophys. Res., 98*, 2949–2956, 1993.

Shettle, E. P., Optical and radiative properties of a desert aerosol model, in *Proceedings of Symposium on Radiation*

in the Atmosphere, edited by G. Fiocco, pp. 74–77, A. Deepak, Hampton, Va., 1984.

Tanré, D., and M. Legrand, On the satellite retrieval of Saharan dust optical thickness over land: Two different approaches, *J. Geophys. Res., 96*, 5221–5227, 1991.

Tanré, D., P. Y. Deschamps, C. Devaux, and M. Herman, Estimation of Saharan aerosol optical thickness from blurring effects in Thematic Mapper data, *J. Geophys. Res., 93*, 15,955–15,964, 1988.

Tegen, I., A. A. Lacis, and I. Fung, The influence on climate forcing of mineral aerosols from disturbed soils, *Nature, 380*, 419–422, 1996.

Teillet, P., Rayleigh optical depth comparisons from various sources, *Appl. Opt., 29*, 1897–1900, 1990.

Vigroux, E., Contribution à l'étude expérimentale de l'absorption de l'ozone, *Ann. Phys., 8*, 709–762, 1953.

World Meterological Organization (WMO), Radiation commission of IAMAP meeting of experts on aerosol and their climatic effects, *WMO Rep. WCP55*, Geneva, 1983.

C. Ichoku, Science Systems and Applications, Inc., Climate and Radiation Branch, Code 913, NASA Goddard Space Flight Center, Greenbelt, MD 20771. (ichoku@climate.gsfc.nasa.gov)

Y. J. Kaufman and L. Remer, Laboratory for Atmospheres, Code 913, NASA Goddard Space Flight Center, Greenbelt, MD 20771. (kaufman@climate.gsfc.nasa.gov; remer@climate.gsfc.nasa.gov)

I. Sabbah, Department of Physics, Faculty of Science, Alexandria University, Alexandria, Egypt. (sabbahsom@yahoo.com)